frontiers | Frontiers in Materials

ORIGINAL RESEARCH
published: 05 July 2022
doi: 10.3389/fmats.2022.934759

Sol–Gel Synthesis and Photocatalytic Activity of Graphene Oxide/$ZnFe_2O_4$-Based Composite Photocatalysts

Beibei Tong, Longfei Shi and Xiaohong Liu*

Department of Mechanical Engineering, Yellow River Conservancy Technical Institute, Kaifeng, China

ZnO (ZO), Fe_2O_3 (FO), and graphene oxide (GO)/ZO/FO/$ZnFe_2O_4$ (ZFO) composite photocatalysts have been synthesized successfully *via* a simple sol–gel method and low-temperature technology. The phase structure and microstructural analysis confirmed that the GO/ZO/FO/ZFO magnetic separation photocatalyst is composed of GO, hexagonal ZnO, rhombohedral Fe_2O_3, and spinel $ZnFe_2O_4$ without any other impurities. The GO/ZO/FO/ZFO composite photocatalysts have a high visible light optical absorption coefficient and photocatalytic activity for degrading dyes, refractory pollutants, and antibiotics. The degradation percentages of methyl orange, tetrabromobisphenol A, and oxytetracycline hydrochloride by the GO/ZO/FO/ZFO magnetic separation photocatalyst were 98% for 180 min, 99% for 150 min, and 85% for 180 min, respectively. The special synthesis path leads to the formation of a special heterojunction between GO, ZnO, Fe_2O_3, and $ZnFe_2O_4$, which does not change the optical band gap value of the main lattice Fe_2O_3, and enhances the surface defects of the GO/ZO/FO/ZFO magnetic separation photocatalyst, resulting in high charge carrier transfer and separation efficiency of the catalyst and then enhanced the photocatalytic activity of the GO/ZO/FO/ZFO magnetic separation photocatalyst.

Keywords: ZnO, Fe_2O_3, composite photocatalysts, sol–gel method, charge carrier, photocatalytic activity

OPEN ACCESS

Edited by:
Steven Wu,
University of South Dakota, United States

Reviewed by:
Tao Xian,
Qinghai Normal University, China
Zuming He,
Changzhou University, China
Zao Yi,
Southwest University of Science and Technology, China

****Correspondence:***
Beibei Tong
t66pp23@163.com

Specialty section:
This article was submitted to Semiconducting Materials and Devices, a section of the journal Frontiers in Materials

Received: *03 May 2022*
Accepted: *26 May 2022*
Published: *05 July 2022*

Citation:
Tong B, Shi L and Liu X (2022) Sol–Gel Synthesis and Photocatalytic Activity of Graphene Oxide/$ZnFe_2O_4$-Based Composite Photocatalysts. Front. Mater. 9:934759. doi: 10.3389/fmats.2022.934759

INTRODUCTION

Environmental pollution has always been a coexisting problem with human development (Rasheed, 2022). Dyes, persistent organic pollutants, and antibiotics are all powerful environmental killers (Cheng et al., 2022; He et al., 2022; Li et al., 2022). The degradation of these pollutants has become a necessary means to protect the environment. As countries around the world attach importance to environmental pollution, different technological means have been developed to degrade these pollutants (He et al., 2019a; He et al., 2021a; Wang et al., 2021a; He et al., 2021b; Wang et al., 2022a; Zhao et al., 2022). These technologies mainly include the photocatalytic technology, thermal catalytic technology, piezoelectric catalytic technology, ultrasonic catalytic technology, electrocatalytic technology, biodegradation technology, and a variety of technologies combined together to degrade pollutants (Sadrameli, 2016; Xiong et al., 2018; He et al., 2019b; He et al., 2020; Cheng et al., 2021; Dadashzadeh et al., 2021). Among these technologies, photocatalysis is a semiconductor green technology driven by light energy, which can effectively degrade pollutants, and has attracted extensive attention from researchers all over the world (Selli et al., 2008). The key

aspect of the semiconductor photocatalysis technology is to develop semiconductor materials that can respond to visible light and use sunlight efficiently (Ren et al., 2016). Therefore, the development of a semiconductor photocatalyst that can respond to visible light becomes the key to solving this problem.

The photocatalytic activity of photocatalyst also depends on its charge carrier transfer and separation efficiency (Tang et al., 2018; Chen et al., 2019a; Cao et al., 2019; Luo et al., 2019; Xiao et al., 2019; Lin et al., 2020; Tang et al., 2020; Wang et al., 2022b). Even if some semiconductor materials can respond to visible light, the transfer and separation efficiency of charge carriers is not high, and Fe_2O_3 is such a material (Kuang et al., 2017; Chong et al., 2021; Fu et al., 2021). In order to enhance the visible light response capability of semiconductor materials and the transfer and separation efficiency of charge carriers at the same time, the excellent properties of various semiconductor materials can be combined to form a new composite semiconductor photocatalyst (Chen et al., 2019b; Shanavas et al., 2019; Kormányos et al., 2020). ZnO (ZO)/Fe_2O_3(FO)/$ZnFe_2O_4$(ZFO) is considered to be such a composite that its visible light response is improved compared with any single component materials (Valenzuela et al., 2002; Karpova et al., 2013a; Karpova et al., 2013b). However, due to the lack of carriers for charge carrier transfer and separation among the three, the transfer and separation efficiency of the charge carrier is low. Graphene oxide (GO) is a common carrier of charge carrier transfer and transport and is often used to enhance the charge transfer and separation efficiency of semiconductor materials (Hosseini et al., 2019; Rahmani et al., 2020; Pei et al., 2021). Therefore, the development of GO/ZO/FO/ZFO composite photocatalysts and the study of their degradation of dyes, POPS, and antibiotics are expected to show high photocatalytic activity.

In this study, we proposed the synthesis of GO/ZO/FO/ZFO composite photocatalysts with different GO contents by a low-temperature sintering technique. The effect of GO content on the phase purity, microstructure, optical properties, and photocatalytic activity of the GO/ZO/FO/ZFO composite photocatalyst was systematically studied. Using methyl orange, tetrabromobisphenol A, and oxytetracycline hydrochloride as degradation materials, the photocatalytic activity of the GO/ZO/FO/ZFO composite photocatalyst was studied. Based on the energy band theory and experimental results, a reasonable photocatalytic mechanism of the GO/ZO/FO/ZFO composite photocatalyst is proposed.

EXPERIMENTAL SECTION

Synthesis of ZnO and Fe_2O_3

According to the stoichiometric ratio of ZnO and Fe_2O_3, zinc nitrate and ferric nitrate were dissolved in 25 ml deionized water, respectively. Solutions containing zinc nitrate and ferric nitrate are labeled as solutions A and B, respectively. After zinc nitrate and ferric nitrate were dissolved, 5 g of citric acid was added to both A and B solutions to make the citric acid react with Zn ions or Fe ions. Then, the A and B solutions were transferred to an oil bath at 300°C for 12 h to obtain a black gel. A and B gels were ground into fine powder in a mortar, and after grinding with urea for half an hour, they were transferred to the combustion network for spontaneous combustion for 2 h to obtain ZnO and Fe_2O_3 powders.

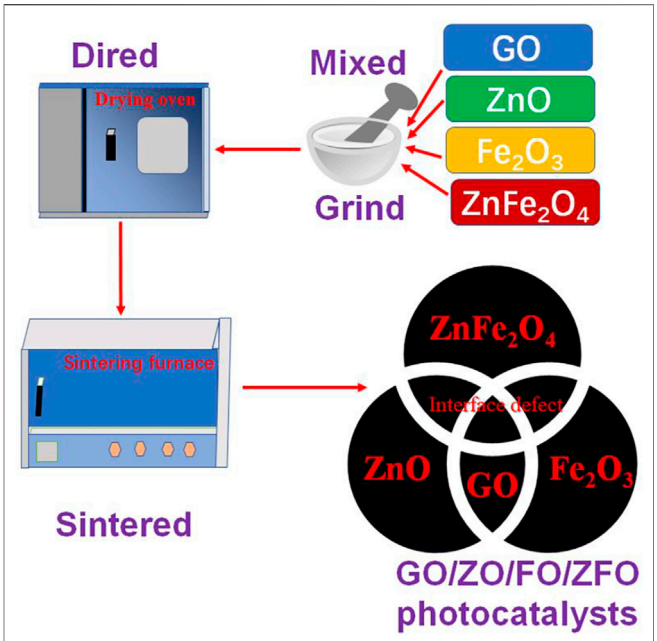

FIGURE 1 | Preparation of the flowchart of GO/ZO/FO/ZFO.

One-Step Low-Temperature Sintering Synthesis of Graphene Oxide/ZnO/Fe_2O_3/$ZnFe_2O_4$ Photocatalysts

Graphene oxide (GO) and $ZnFe_2O_4$ (ZFO) were purchased from Aladdin Reagent LTD. According to Guskos et al. (2010), ZO/FO/ZFO with the mass ratio of ZO: FO: ZFO = 20 wt%: 10 wt%: 70 wt % was obtained. Then, according to the GO mass ratios of 5 wt%, 10 wt%, 15 wt%, and 20 wt% to ZO/FO/ZFO, they are named GO/ZO/FO/ZFO1, GO/ZO/FO/ZFO2, GO/ZO/FO/ZFO3, and GO/ZO/FO/ZFO4, respectively. Finally, the samples were placed in a box furnace and sintered at 200°C for 2 h to obtain the final sample. **Figure 1** shows the preparation flowchart of GO/ZO/FO/ZFO.

Material Characterization

The phase structures of samples GO, ZnO, Fe_2O_3, GO/ZO/FO/ZFO1, GO/ZO/FO/ZFO2, GO/ZO/FO/ZFO3, and GO/ZO/FO/ZFO4 were measured by means of X-ray powder diffraction (XRD) with Cu Kα radiation. The Fourier transform infrared (FTIR) spectrophotometer with Bruker IFS 66v/S was used to study the samples GO, ZnO, Fe_2O_3, GO/ZO/FO/ZFO1, GO/ZO/FO/ZFO2, GO/ZO/FO/ZFO3, and GO/ZO/FO/ZFO4 in the wave-number range of 400–4000 cm^{-1}. The microstructures of GO/ZO/FO/ZFO1, GO/ZO/FO/ZFO2, GO/ZO/FO/ZFO3, and GO/ZO/FO/ZFO4 were investigated by field-emission scanning

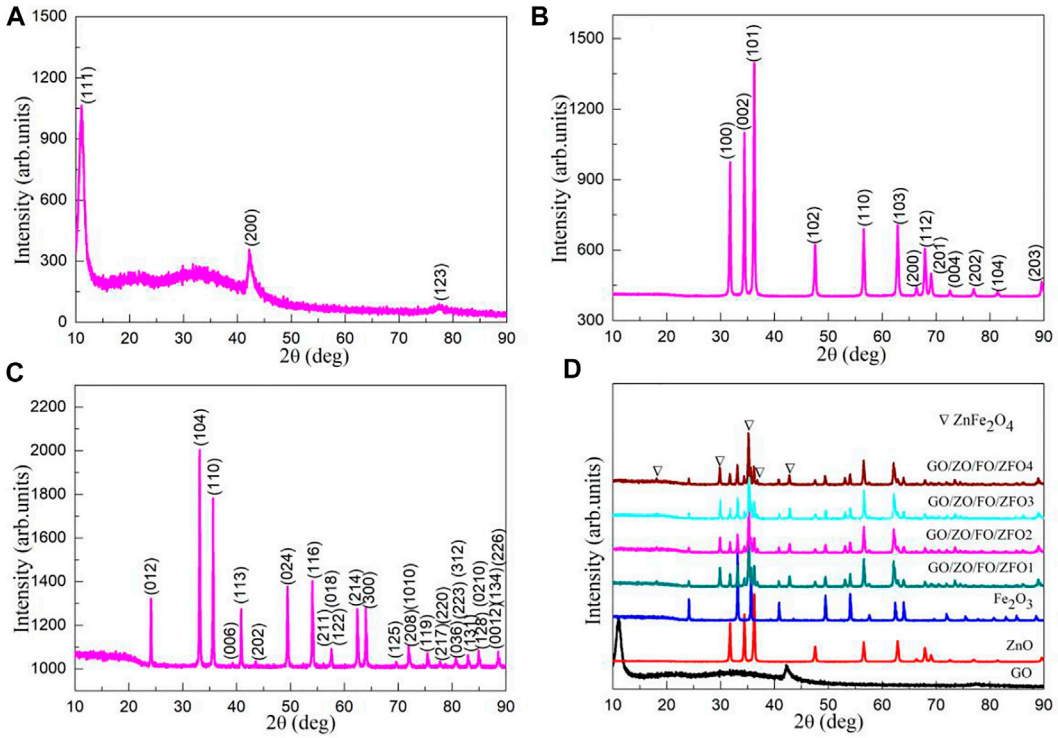

FIGURE 2 | XRD patterns of samples **(A)** GO, **(B)** ZnO, **(C)** Fe_2O_3, **(D)** GO/ZO/FO/ZFO1, GO/ZO/FO/ZFO2, GO/ZO/FO/ZFO3, and GO/ZO/FO/ZFO4.

electron microscopy (SEM) and transmission electron microscopy (TEM). Ultraviolet-visible (UV-Vis) diffuse reflectance spectra of samples GO, ZnO, Fe_2O_3, GO/ZO/FO/ZFO1, GO/ZO/FO/ZFO2, GO/ZO/FO/ZFO3, and GO/ZO/FO/ZFO4 were measured by using a UV1901 UV-Visible spectrophotometer.

Photocatalytic Experiments for the Degradation of Methyl Orange, Tetrabromobisphenol A, and Oxytetracycline Hydrochloride

The photocatalytic activity of GO/ZO/FO/ZFO composite photocatalysts was studied using methyl orange, tetrabromobisphenol A, and oxytetracycline hydrochloride as degradation materials. The light source, initial pollutant concentration, and catalyst concentration were xenon lamps with 500 W, 20 mg/L for methyl orange, 50 mg/L for tetrabromobisphenol A, and 1 g/L for oxytetracycline hydrochloride, respectively. Including adsorption experiments, samples were taken every 30 min, and each photocatalytic experiment was performed for 210 min. The removed solution was centrifuged, and its absorbance was measured by using a UV-Vis spectrophotometer. The photocatalytic degradation rate, first-order kinetic curve, and degradation percentage of the GO/ZO/FO/ZFO magnetic separation photocatalyst can be calculated based on the measured absorbance value.

RESULTS AND DISCUSSION

X-Ray Powder Diffraction Analysis

The phase structure and purity of semiconductor materials are measured by using an X-ray powder diffraction (XRD) instrument to determine whether the synthesized product is the target product. **Figure 2** shows the XRD patterns of samples GO, ZnO, Fe_2O_3, GO/ZO/FO/ZFO1, GO/ZO/FO/ZFO2, GO/ZO/FO/ZFO3, and GO/ZO/FO/ZFO4. The XRD pattern of sample GO (**Figure 2A**) shows the XRD characteristic peaks located at 10.905, 42.193, and 77.772° related to (111), (200), and (123), respectively, which is identical to the JCPDS No. 89-8489. Similarly, ZnO (**Figure 2B**) displays an XRD pattern identical to the hexagonal structural phase with the space group P63mc (186), and the XRD characteristic peaks at 31.736°, 34.378°, 36.214°, 47.483°, 56.534°, 62.775°, 66.302°, 67.886°, 69.007°, 72.462°, 76.865°, 81.268°, and 89.489° related to (100), (002), (101), (102), (110), (103), (200), (112), (201), (004), (202), (104), and (203) crystal plane ZnO corresponds to the JCPDS No. 76-0704. The sample of Fe_2O_3 (**Figure 2C**) exhibits several characteristic peaks located at 2θ of 24.149°, 33.158°, 35.631°, 39.283°, 40.862°, 43.508°, 49.462°, 54.069°, 56.159°, 57.448°, 57.597°, 62.436°, 64.000°, 66.031°, 69.595°, 71.947°, 72.281°, 75.191°, 75.455°, 77.738°, 78.776°, 79.486°, 80.582°, 80.709°, 82.953°, 84.485°, 84.934°, and 88.557°, corresponding to the (012), (104), (110), (006), (113), (202), (024), (116), (211), (122), (018), (214), (300),

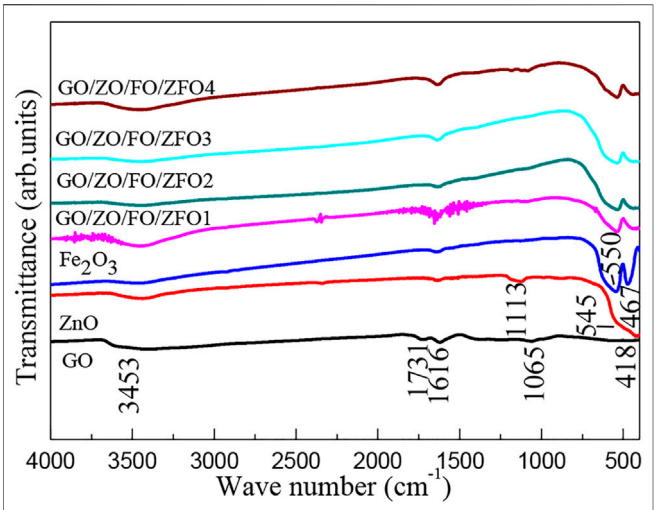

FIGURE 3 | FTIR spectra of samples GO, ZnO, Fe_2O_3, GO/ZO/FO/ZFO1, GO/ZO/FO/ZFO2, GO/ZO/FO/ZFO3, and GO/ZO/FO/ZFO4.

(125), (208), (1010), (119), (217), (220), (036), (223), (131), (312), (128), (0210), (0012), (134), and (226) crystal surfaces of rhombohedral structural Fe_2O_3 with the JCPDS No. 87-1164. When GO, ZnO, Fe_2O_3 and $ZnFe_2O_4$ are combined together, ZnO, Fe_2O_3 and $ZnFe_2O_4$ peaks appear in GO/ZO/FO/ZFO1, GO/ZO/FO/ZFO2, GO/ZO/FO/ZFO3, and GO/ZO/FO/ZFO4, as shown in **Figure 2D**. However, the diffraction peak of GO is difficult to observe. As the GO content increased to 20%, only a weak diffraction peak was observed at 10.905° of the sample GO/ZO/FO/ZFO4, further confirming that GO exists in the sample GO/ZO/FO/ZFO4.

Fourier Transform Infrared Analysis

In order to further study the phase structure and purity of semiconductor materials, FTIR was performed. **Figure 3** shows the FTIR spectra of samples GO, ZnO, Fe_2O_3, GO/ZO/FO/ZFO1, GO/ZO/FO/ZFO2, GO/ZO/FO/ZFO3, and GO/ZO/FO/ZFO4. For all samples, the peaks at 3453 and 1616 cm^{-1} can be ascribed to the absorbed water due to the use of KBr in the tablet pressing process (Gao et al., 2021; Li et al., 2021; Liu et al., 2022). For the sample GO, the peaks at 1731 and 1065 cm^{-1} can be assigned to the graphene oxide (Dat et al., 2022; Hwa et al., 2022). For ZnO, the peaks at 1113, 545, and 418 cm^{-1} are attributed to the characteristic peak of C-O and the Zn–O and Zn-O-Zn vibrations, respectively (Prabhu et al., 2018; Rammah et al., 2020; Wang et al., 2021b; Nadeem et al., 2021; Wang et al., 2022c; Tang et al., 2022). For Fe_2O_3, the peaks at 550 and 467 cm^{-1} are assigned to the Fe-O and Fe-O-Fe vibrations, respectively (Lv et al., 2010; Ratep and Kashif, 2021). For the samples GO/ZO/FO/ZFO, the intensity of the characteristic peak of GO increases with the increase in the GO content, and the characteristic peak of Fe_2O_3 is slightly shifted, especially due to the influence of the Fe-O functional group in $ZnFe_2O_4$ (can be written as $ZnO{\bullet}Fe_2O_3$), and the heterojunction between GO, ZnO, Fe_2O_3, and $ZnFe_2O_4$ is formed.

XPS Analysis

Figure 4A shows the XPS survey spectrum of the sample GO/ZO/FO/ZFO3. The survey spectra of the samples GO/ZO/FO/ZFO3 exhibit sharp peaks of C, Zn, Fe, and O elements, and no other elements are observed, indicating that the sample GO/ZO/FO/ZFO3 does not contain any impurities. **Figure 4B** shows the high-resolution XPS spectrum of Zn 2p for the sample GO/ZO/FO/ZFO3. The two bands of Zn 2p1/2 and 2p3/2 were recorded at 1044.61 and 1021.42 eV, respectively, in $ZnFe_2O_4$, while the peaks at 1024.74 and 1047.77 eV can be ascribed to Zn 2p1/2 and 2p3/2 in ZnO, respectively. The Fe 2p spectrum showed obvious peaks at 711.83 (Fe 2p3/2) and 727.24 (Fe 2p1/2) eV which may be attributed to Fe_2O_3, and the peaks at 714.03 (Fe 2p3/2) and 733.85 (Fe 2p1/2) eV can be assigned to $ZnFe_2O_4$, as shown in **Figure 4C**. The O 1s spectrum of the samples GO/ZO/FO/ZFO3 is displayed in **Figure 4D**. The O1s peak could be convoluted into five peaks at 535.75, 533.51, 531.65, 530.70, and 530.21 eV, respectively. These peaks can be ascribed to C-O, the lattice oxygen of ZnO (O-Zn-ZO), the lattice oxygen of $ZnFe_2O_4$ (O-Zn-ZFO), the lattice oxygen of Fe_2O_3 (O-Zn-FO), and the lattice oxygen of $ZnFe_2O_4$ (O-Fe-ZFO), respectively. **Figure 4E** shows the high-resolution XPS spectra of C1s for the sample GO/ZO/FO/ZFO3. Three peaks at 287.72, 285.32, and 283.49 eV can be assigned C-H, C-O, and C1s for the XPS calibration peak, respectively. The results further confirmed the successful synthesis of the GO/ZO/FO/ZFO photocatalyst by low-temperature sintering technology.

Microstructural Analysis

The microstructure of semiconductor material has a great influence on its photocatalytic activity. **Figures 5A–D** show the SEM images of samples GO/ZO/FO/ZFO1, GO/ZO/FO/ZFO2, GO/ZO/FO/ZFO3, and GO/ZO/FO/ZFO4. When the GO content is 5%, the samples are mainly composed of fine nanoparticles, with lamellar particles faintly visible, as shown in **Figure 5A**. When the content of GO increased to 10%, the agglomeration of fine particles became obvious, and the lamellar structure gradually increased, as shown in **Figure 5B**. When the content of GO further increased to 15%, fine nanoparticles gradually deposited on GO, and the lamellar structure became more obvious, as shown in **Figure 5C**. With the GO content reaching 20%, lamellar structures appear in the samples in large quantities, as shown in **Figure 5D**. **Figures 5E,F** show the TEM and HRTEM images of the sample GO/ZO/FO/ZFO3, respectively. It can be seen from **Figure 5E** that fine nanoparticles are deposited on the lamellar GO, which is consistent with the SEM observation result. The lattice planes of ZnO, Fe_2O_3, and $ZnFe_2O_4$ were (100) and (101) with a lattice space of 0.2827 and 0.2486 nm, respectively, (104) and (110) with a lattice space of 0.2699 and 0.2517 nm, respectively, and (311) with a lattice space of 0.2536 nm, respectively. The results further confirmed that the GO/ZO/FO/ZFO3 samples contained GO, ZnO, Fe_2O_3, and $ZnFe_2O_4$.

Optical Properties

The optical properties can be used to determine whether the semiconductor material has a high optical absorption

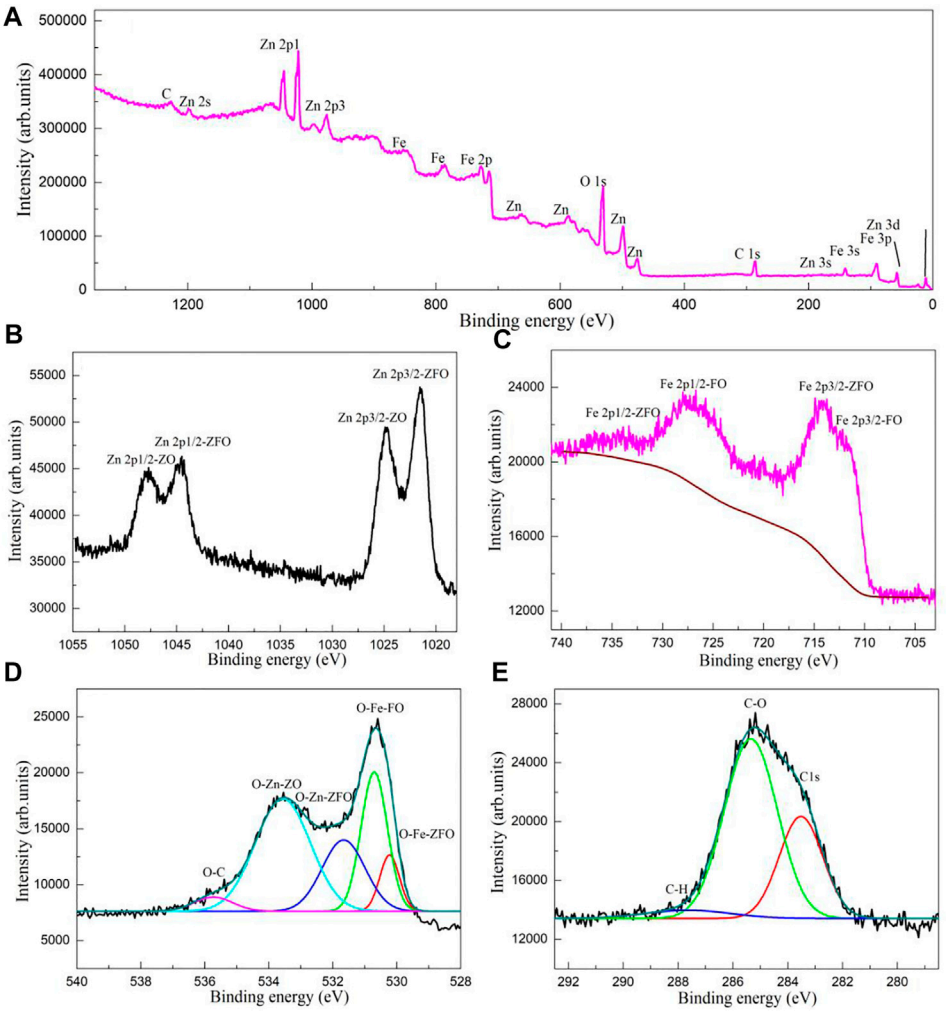

FIGURE 4 | (A) XPS survey spectrum and high-resolution XPS spectra of **(B)** Zn 2p, **(C)** Fe 2p, **(D)** O 1s, and **(E)** C 1s for the sample GO/ZO/FO/ZFO3.

coefficient and further verify whether it has high photocatalytic activity. **Figure 6A** shows the UV-Vis diffuse reflectance spectra of samples GO, ZnO, Fe_2O_3, GO/ZO/FO/ZFO1, GO/ZO/FO/ZFO2, GO/ZO/FO/ZFO3, and GO/ZO/FO/ZFO4. Fe_2O_3 has the lowest reflectivity, and ZnO has the highest reflectivity in the wavelength range of 400–800 nm, while GO tends to be almost constant in this range. When GO, ZnO, Fe_2O_3, and $ZnFe_2O_4$ are coupled, the reflectivity in the visible light range changes significantly compared with ZnO and is greatly improved. After 850 nm, the reflectivity of GO/ZO/FO/ZFO samples increases sharply with the increase in wavelength.

According to Kubelka–Munk's (K–M) formula, the UV-Vis diffuse reflectance spectrum can be transformed into the UV-Vis absorption spectrum.

$$F(R) = \frac{\alpha}{S} = \frac{(1 - R_\infty)^2}{2R} \quad (1)$$

where R is the reflectance of samples GO, ZnO, Fe_2O_3, GO/ZO/FO/ZFO1, GO/ZO/FO/ZFO2, GO/ZO/FO/ZFO3, and GO/ZO/FO/ZFO4, α is the optical absorption coefficient, and S is the scattering coefficient of samples GO, ZnO, Fe_2O_3, GO/ZO/FO/ZFO1, GO/ZO/FO/ZFO2, GO/ZO/FO/ZFO3, and GO/ZO/FO/ZFO4. **Figure 6B** shows the UV-Vis absorption spectra of samples GO, ZnO, Fe_2O_3, GO/ZO/FO/ZFO1, GO/ZO/FO/ZFO2, GO/ZO/FO/ZFO3, and GO/ZO/FO/ZFO4. ZnO exhibits a high UV absorption coefficient, indicating that it has high UV photocatalytic activity. Fe_2O_3 has the highest light absorption coefficient in the wavelength range of 190–900 nm, but its photocatalytic activity is not high because of its high charge carrier recombination rate. When GO, ZnO, Fe_2O_3 and $ZnFe_2O_4$ are coupled to form heterojunctions, the absorption coefficient of the GO/ZO/FO/ZFO sample is greatly improved in the visible light range compared with ZnO, indicating that GO/ZO/FO/ZFO samples have high visible-light photocatalytic activity.

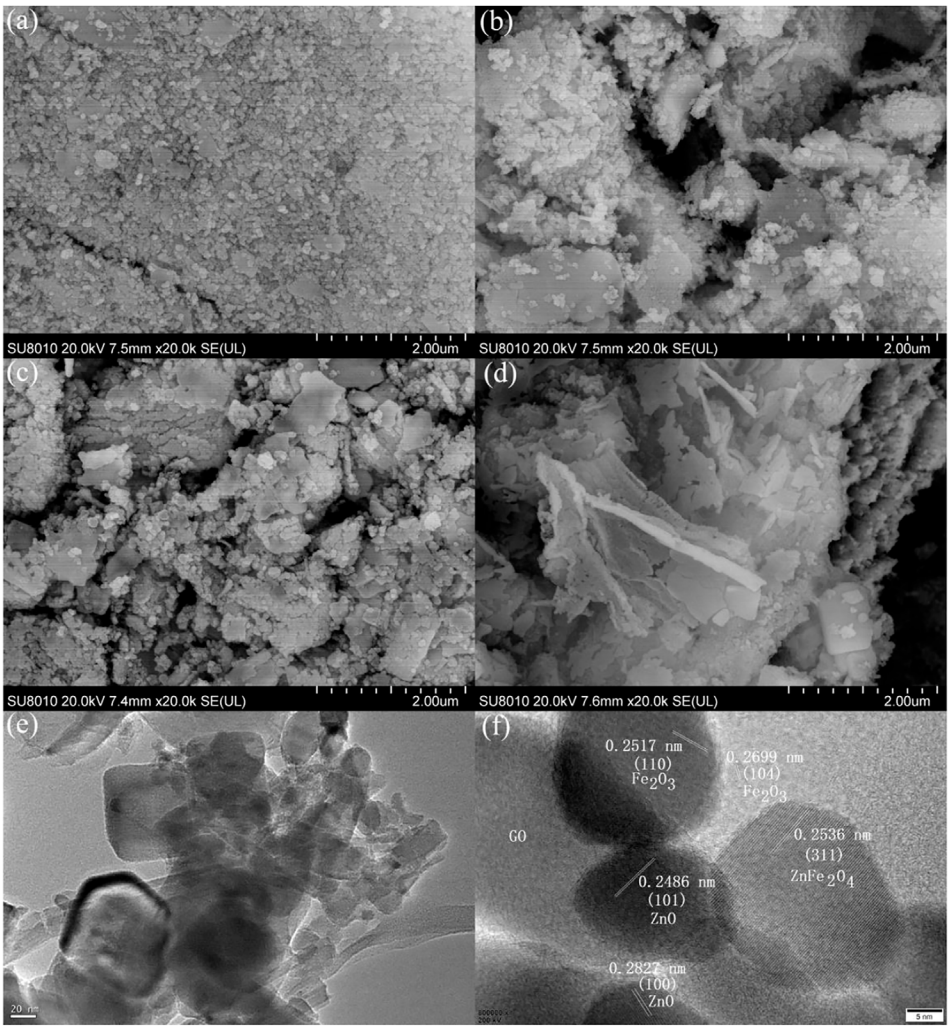

FIGURE 5 | SEM images of samples **(A)** GO/ZO/FO/ZFO1, **(B)** GO/ZO/FO/ZFO2, **(C)** GO/ZO/FO/ZFO3, and **(D)** GO/ZO/FO/ZFO4. **(E)** TEM and **(F)** HRTEM images of the sample GO/ZO/FO/ZFO3.

The first-order differential curve is calculated based on the UV-vis diffuse reflectance spectrum. The peak of the curve can be used to obtain the optical band gap (Eg) value of the semiconductor material (Gao et al., 2019; Gao et al., 2022a).

$$E_g\,(\mathrm{eV}) = \frac{hc}{\lambda_0\,(\mathrm{nm})} \approx \frac{1240}{\lambda_0\,(\mathrm{nm})} \tag{2}$$

where λ_0, h, and c are the peak of the first-order differential curve, the Plank constant, and the velocity of light, respectively. **Figures 6C–F** show the first-order differential curves of UV-Vis diffuse reflectance spectra of samples GO, ZnO, Fe_2O_3, GO/ZO/FO/ZFO1, GO/ZO/FO/ZFO2, GO/ZO/FO/ZFO3, and GO/ZO/FO/ZFO4. The Eg values of samples GO, ZnO, Fe_2O_3, GO/ZO/FO/ZFO1, GO/ZO/FO/ZFO2, GO/ZO/FO/ZFO3, and GO/ZO/FO/ZFO4 are 1.44, 3.18, 2.12, 2.11, 2.11, 2.11, and 2.11 eV, respectively. As can be seen from **Figure 5F**, when GO, ZnO, Fe_2O_3 and $ZnFe_2O_4$ are coupled, the Eg value does not change at all. According to Xue et al. (2019), Kelaidis et al. (2020), Wang et al. (2021c), Gao et al. (2022b), and Gao et al. (2022c), only defects or vacancies can be introduced, and their Eg values will not be changed after a variety of semiconductor photocatalysts are coupled to form heterojunctions. This result is consistent with the literature reports.

Photocatalytic Activity for the Degradation of Dyes

The photocatalytic activity of the sample GO/ZO/FO/ZFO was studied with dyes, pollutants, and antibiotics as target degradation materials. **Figure 7A** shows the time-dependent degradation of methyl orange in the presence of the sample GO/ZO/FO/ZFO3 under simulated solar irradiation. Before the photocatalytic degradation experiment, methyl orange was adsorbed for half an hour to exclude the influence of adsorption on photocatalytic activity. After half an hour of adsorption, the

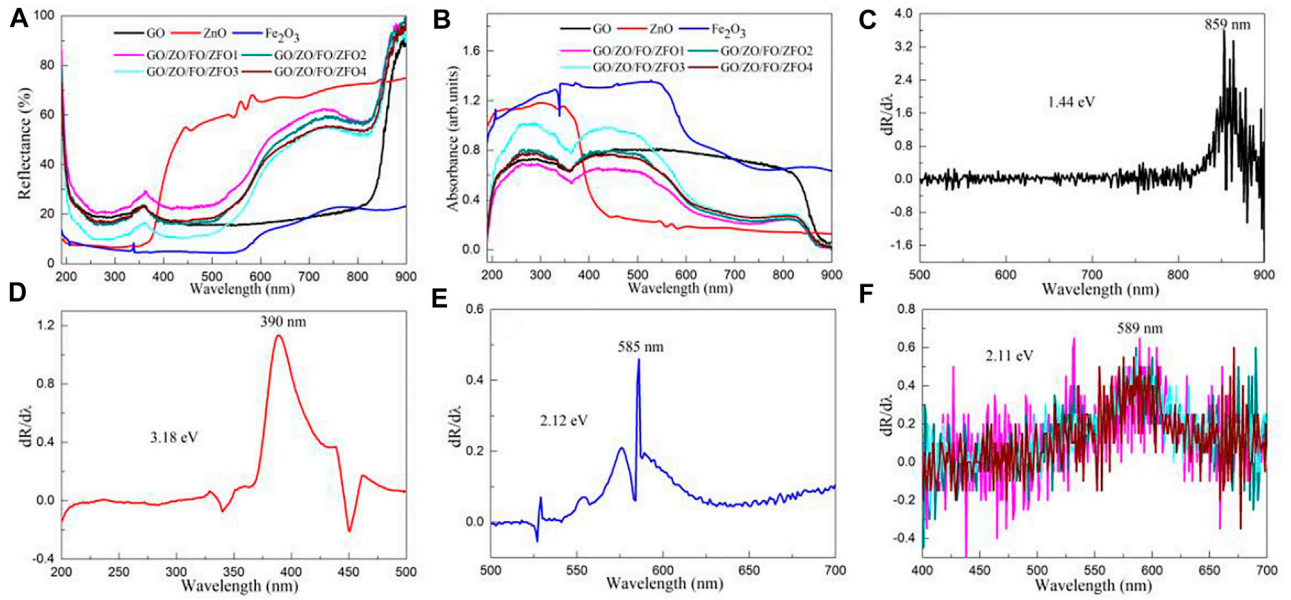

FIGURE 6 | (A) UV-Vis diffuse reflectance spectra and **(B)** UV-Vis absorption spectra of samples GO, ZnO, Fe_2O_3, GO/ZO/FO/ZFO1, GO/ZO/FO/ZFO2, GO/ZO/FO/ZFO3, and GO/ZO/FO/ZFO4. First-order differential curves of UV-Vis diffuse reflectance spectra of samples **(C)** GO, **(D)** ZnO, **(E)** Fe_2O_3, **(F)** GO/ZO/FO/ZFO1, GO/ZO/FO/ZFO2, GO/ZO/FO/ZFO3, and GO/ZO/FO/ZFO4.

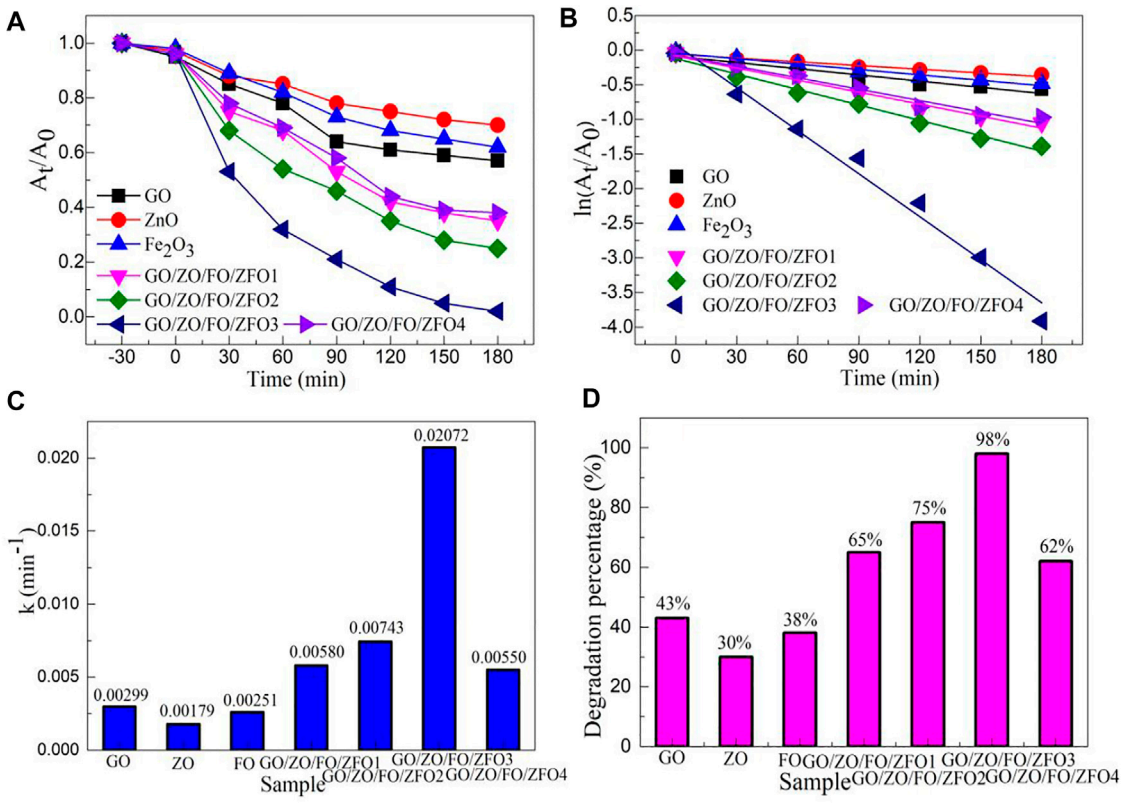

FIGURE 7 | (A) Time-dependent characteristic, **(B)** plots of ln (A_t/A_0) vs. irradiation time (t), **(C)** first-order kinetic constant (k), and **(D)** degradation percentage of degradation of methyl orange in the presence of samples GO, ZnO, Fe_2O_3, and GO/ZO/FO/ZFO under simulated solar irradiation.

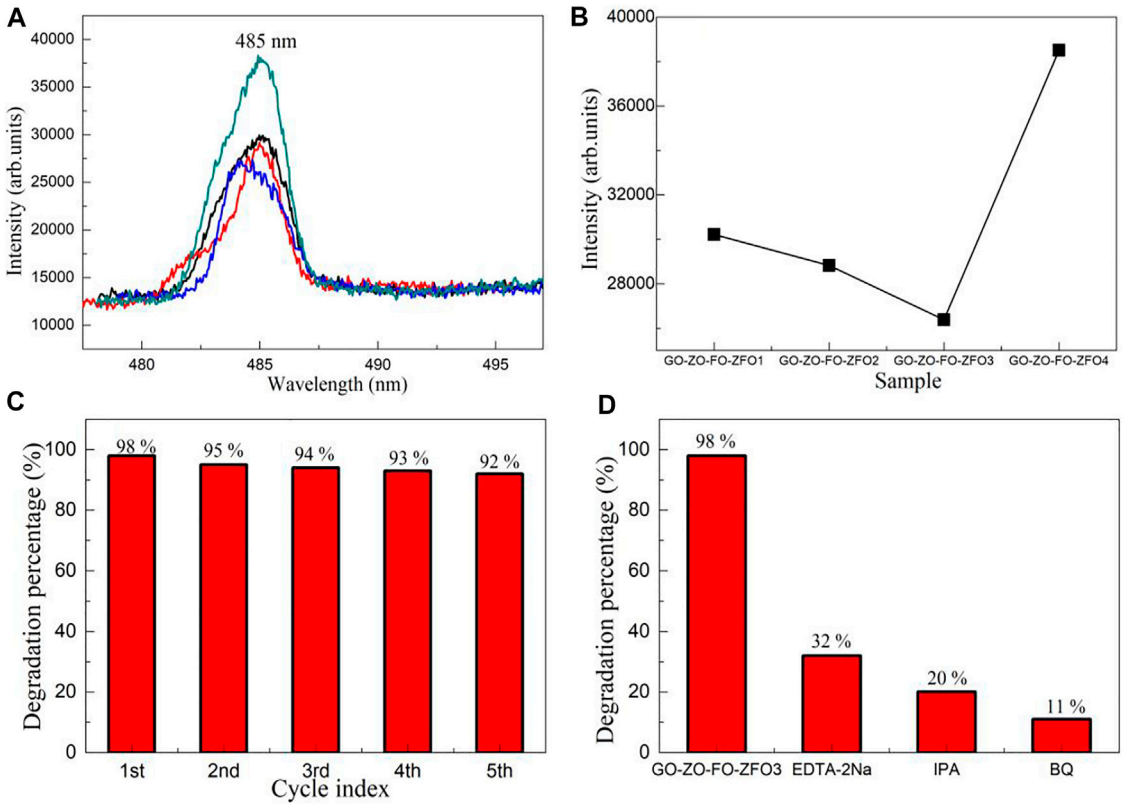

FIGURE 8 | (A) Emission spectra (λex = 300 nm) of the GO/ZO/FO/ZFO photocatalyst. **(B)** Maximum emission intensity at 485 nm of the GO/ZO/FO/ZFO photocatalyst. The **(C)** stability and **(D)** trapping experiments of the GO/ZO/FO/ZFO3 photocatalyst.

adsorption of methyl orange by GO, ZnO, Fe_2O_3, and GO/ZO/FO/ZFO is small, less than 10%. The degradation rate of all samples increased with the increase in illumination time. Under visible light irradiation, the photocatalytic degradation percentage of GO, ZnO, and Fe_2O_3 is less than 30%. The sample GO/ZO/FO/ZFO3 showed the highest photocatalytic activity, and the degradation percentage reached 98% after 3 h of degradation.

The first-order kinetic curve can directly reflect the photocatalytic activity of semiconductor materials. The first-order dynamics equation can be described as follows:

$$\ln(A_t/A_0) = -Kt, \quad (3)$$

where A_t is the absorbance of the pollutant at time t, A_0 is the absorbance of the pollutant at the initial time, k is the first-order kinetic constant, and t is the irradiation time. **Figure 7B** shows the plots of ln (A_t/A_0) vs. irradiation time of degradation of methyl orange in the presence of the sample GO/ZO/FO/ZFO3 under simulated solar irradiation. ln (A_t/A_0) for samples GO, ZnO, Fe_2O_3, and GO/ZO/FO/ZFO shows a good linear relationship with the irradiation time. **Figure 7C** shows the k values of degradation of methyl orange in the presence of samples GO, ZnO, Fe_2O_3, and GO/ZO/FO/ZFO under simulated solar irradiation. The k values of samples GO, ZnO, Fe_2O_3, GO/ZO/FO/ZFO1, GO/ZO/FO/ZFO2, GO/ZO/FO/ZFO3, and GO/ZO/FO/ZFO4 are 0.00299, 0.00179, 0.00251, 0.00580, 0.00743, 0.02072, and 0.00550 min^{-1}, respectively. The photocatalytic degradation rate of GO/ZO/FO/ZFO3 is 11.58 times that of ZnO. **Figure 7D** shows the degradation percentage of degradation of methyl orange in the presence of samples GO, ZnO, Fe_2O_3, and GO/ZO/FO/ZFO under simulated solar irradiation. The degradation percentages of samples GO, ZnO, Fe_2O_3, GO/ZO/FO/ZFO1, GO/ZO/FO/ZFO2, GO/ZO/FO/ZFO3, and GO/ZO/FO/ZFO4 are 43%, 30%, 38%, 65%, 75%, 98%, and 62%, respectively. With the increase in the GO content, the photocatalytic velocity of the GO/ZO/FO/ZFO photocatalyst first increases and then decreases. The results further confirmed that the sample GO/ZO/FO/ZFO3 had the highest photocatalytic activity.

Stability and Trapping Experiments

Figure 8A shows the emission spectra (λex = 300 nm) of the GO/ZO/FO/ZFO photocatalyst. The GO/ZO/FO/ZFO photocatalyst showed a narrow fluorescence emission peak at 485 nm, which may be caused by GO (Iliut et al., 2013; El-Hnayn et al., 2020). The maximum emission intensity at 485 nm of the GO/ZO/FO/ZFO photocatalyst is shown in **Figure 8B**. Compared with the photocatalytic activity, the emission intensity decreased with the

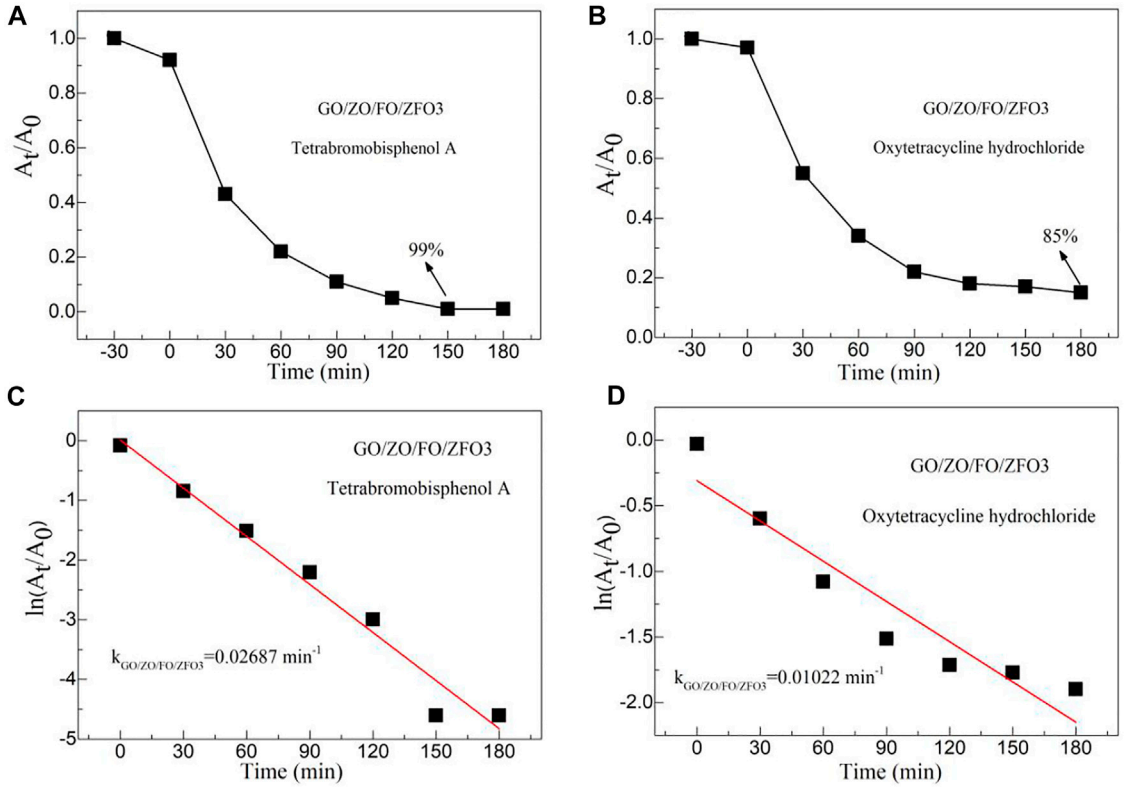

FIGURE 9 | Time-dependent degradation of **(A)** tetrabromobisphenol A and **(B)** oxytetracycline hydrochloride in the presence of the sample GO/ZO/FO/ZFO3 under simulated solar irradiation. Plots of ln (A_t/A_0) vs. irradiation time (t) for the degradation of **(C)** tetrabromobisphenol A and **(D)** oxytetracycline hydrochloride in the presence of the sample GO/ZO/FO/ZFO3.

increase in the photocatalytic activity. It can be seen from the fluorescence emission spectrum that the photocatalyst exhibits poor transfer and separation rates of photogenerated carriers with higher emission intensity. To study the stability of the GO/ZO/FO/ZFO photocatalyst, **Figure 8C** shows the stability experiments of the GO/ZO/FO/ZFO3 photocatalyst. After five cycles, the photocatalytic activity of the GO/ZO/FO/ZFO3 photocatalyst decreased by less than 6%, indicating that the GO/ZO/FO/ZFO3 photocatalyst has high stability and recycling ability. The trapping experiments of the GO/ZO/FO/ZFO3 photocatalyst are shown in **Figure 8D**. Trapping agents include the disodium ethylenediamine tetraacetic acid (EDTA-2Na), 2-propanol (IPA), and 1,4-benzoquinone (BQ), which have been used to detect the hole (h_{VB}^+), hydroxyl radical (•OH), and superoxide radical ($•O_2^-$), respectively. During each photocatalytic experiment, the amount of the trapping agent added to the reaction solution was 1 mmol/L. When EDTA-2Na, IPA, and BQ were added to the reaction solution, the photocatalytic activity of the GO/ZO/FO/ZFO3 photocatalyst decreased to 32%, 20%, and 11%, respectively. The results showed that holes, hydroxyl radicals, and superoxide radicals play important roles in the photocatalytic reaction. This will provide strong evidence for the subsequent analysis of the photocatalytic mechanism.

Photocatalytic Activity for the Degradation of Pollutants and Antibiotics

Figures 9A,B show the time-dependent degradation of tetrabromobisphenol A and oxytetracycline hydrochloride in the presence of the sample GO/ZO/FO/ZFO3 under simulated solar irradiation, respectively. The degradation percentage of GO/ZO/FO/ZFO3 to tetrabromobisphenol A reached 99% after 150 min and that of oxytetracycline hydrochloride reached 85% after 180 min. The results showed that the sample GO/ZO/FO/ZFO3 had a high photocatalytic activity for the degradation of refractory pollutants and antibiotics. **Figures 9C,D** show the plots of ln (A_t/A_0) vs. irradiation time (t) for the degradation of tetrabromobisphenol A and oxytetracycline hydrochloride in the presence of the sample GO/ZO/FO/ZFO3, respectively. The k-values of the sample GO/ZO/FO/ZFO3 for the degradation of tetrabromobisphenol A and oxytetracycline hydrochloride are 0.02687 and 0.01022 min^{-1}, respectively. The results showed that the sample GO/ZO/FO/ZFO3 had the highest photocatalytic activity for the degradation of tetrabrombisphenol A.

Photocatalytic Mechanism

In order to gain insight into the photocatalytic mechanism of GO/ZO/FO/ZFO, the conduction band potential (E_{CB}) and

TABLE 1 | Conduction band, valence band potential, electronegativity, and Eg values of GO, ZnO and Fe_2O_3, and $ZnFe_2O_4$.

Sample	Eg (eV)	X (eV)	E_{CB} (eV)	E_{VB} (eV)
GO	1.44	6.91	1.69	3.13
ZnO	3.18	5.79	–0.30	2.88
Fe_2O_3	2.12	5.89	0.33	2.45
$ZnFe_2O_4$	1.71	5.86	0.51	2.22

valence band (E_{VB}) potential of GO, ZnO, Fe_2O_3 and $ZnFe_2O_4$ were calculated based on the band theory. **Table 1** shows the conduction band, valence band potential, electronegativity, and Eg values of GO, ZnO, Fe_2O_3, and $ZnFe_2O_4$.

$$E_{CB} = X - E^e - 0.5E_g \quad (4)$$

$$E_{VB} = E_{CB} + E_g \quad (5)$$

where the Eg values of GO, ZnO,Fe_2O_3, and $ZnFe_2O_4$ are 1.44, 3.18, 2.12, and 1.71 eV (Wang et al., 2019), respectively. E^e is 4.5 eV. The absolute electronegativity (X) values of GO, ZnO, Fe_2O_3, and $ZnFe_2O_4$ are 6.91, 5.79, 5.89, and 5.86 eV, respectively, and can be evaluated by **Eqs. 4**, **5**.

$$X\left(C_4O_{2-x}(OH)_{2x}(x=0.1)\right) = \sqrt[6,3]{X^4(C)*X^{2.1}(O)*X^{0.2}(H)} \quad (6)$$

$$X(ZnO) = \sqrt[2]{X(Zn)*X(O)} \quad (7)$$

$$X(Fe_2O_3) = \sqrt[5]{X^2(Fe)*X^3(O)} \quad (8)$$

$$X(ZnFe_2O_4) = \sqrt[7]{X(Zn)*X^2(Fe)*X^4(O)} \quad (9)$$

where X (C) = 6.27 eV, X (H) = 7.18 eV, X (Zn) = 4.45 eV, X (Fe) = 4.06 eV, and X (O) = 7.54 eV.

Based on the aforementioned calculations, the energy level diagram of GO/ZO/FO/ZFO is shown in **Figure 10**. As can be seen from the figure, GO acts as a carrier of charge transfer and transmission between ZnO, Fe_2O_3, and $ZnFe_2O_4$. When light is illuminated on the surface of the GO/ZO/FO/ZFO composite, the electrons in the respective valence band undergo transition to the conduction band. Since the conduction band of GO is more negative than ZnO, Fe_2O_3 and $ZnFe_2O_4$, the electrons will relax to the conduction band of GO. The valence bands of GO are more positive than those of ZnO, Fe_2O_3, and $ZnFe_2O_4$, and the valence band holes will undergo transition to the valence bands of ZnO, Fe_2O_3, and $ZnFe_2O_4$. Such relaxation and transition will promote the separation of electron and hole pairs of the whole complex, resulting in a large increase in its photocatalytic activity. The conduction electrons will react with oxygen in the reactant solution to form superoxide radicals and with $O_2/2H^+$ to form hydroxyl radicals. Valence band holes will react with H_2O/OH^- to form hydroxyl radicals. Subsequently, hydroxyl radicals or superoxide radicals react with pollutants to form non-toxic and harmless small organic molecules. Meanwhile, the valence band holes may react directly with pollutants to form non-toxic and harmless small molecular organics. The related chemical reactions can be expressed as follows:

$$GO/ZO/FO/ZFO + hv \rightarrow e^- + h^+ \quad (10)$$

$$h^+ + OH^- \rightarrow \cdot OH \quad (11)$$

$$e^- + O_2 \rightarrow \cdot O^{2-} \quad (12)$$

$$\cdot O^{2-} + 2H^+ + e^- \rightarrow H_2O_2 \quad (13)$$

$$2e^- + O_2 + 2H^+ \rightarrow H_2O_2 \quad (14)$$

$$e^- + H_2O_2 \rightarrow \cdot OH + OH^- \quad (15)$$

$$\cdot O^{2-} + H_2O_2 \rightarrow \cdot OH + OH^- + O_2 \quad (16)$$

$$\cdot OH/\cdot O^{2-} + dye/Pollutant/antibiotics \rightarrow degradation\ products \quad (17)$$

$$h^+ + dye/pollutant/antibiotics \rightarrow degradation\ products \quad (18)$$

It can be seen that the holes, hydroxyl radicals, and superoxide radicals play important roles in the whole photocatalytic process.

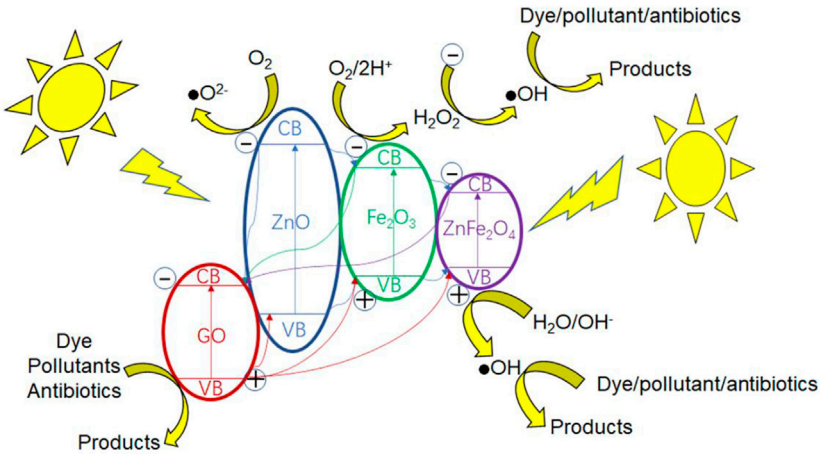

FIGURE 10 | Photocatalytic mechanism of GO/ZO/FO/ZFO.

CONCLUSION

GO/ZO/FO/ZFO composite photocatalysts with different GO contents were synthesized by a low-temperature sintering technique. The effects of the GO content on the phase purity, functional groups, microstructure, optical properties, and photocatalytic activity of GO/ZO/FO/ZFO composite photocatalysts were studied in detail. XRD, FTIR, and microstructural analysis confirmed that the GO/ZO/FO/ZFO magnetic separation photocatalyst contains four components, GO, ZnO, Fe_2O_3, and $ZnFe_2O_4$, without any other impurities. The optical property analysis shows that the GO/ZO/FO/ZFO magnetic separation photocatalyst has a high optical absorption coefficient, suggesting that it has a high visible-light photocatalytic activity, and the quadruple recombination does not change the Eg value of the main lattice of Fe_2O_3. The photocatalytic experiments confirmed that the GO/ZO/FO/ZFO magnetic separation photocatalyst had high photocatalytic activity for dyes, refractory pollutants, and antibiotics, and the degradation percentages were 98% for 180 min, 99% for 150 min, and 85% for 180 min, respectively. The special heterojunction structure promotes the transfer and separation of electrons and holes in the GO/ZO/FO/ZFO magnetic separation photocatalyst, showing high photocatalytic activity under the combined action of holes, hydroxyl radicals, and superoxide radicals.

DATA AVAILABILITY STATEMENT

The raw data supporting the conclusions of this article will be made available by the authors, without undue reservation.

AUTHOR CONTRIBUTIONS

All authors listed have made a substantial, direct, and intellectual contribution to the work and approved it for publication.

FUNDING

This work was supported by the Core Teacher Cultivating Program of the Yellow River Conservancy Technical Institute (No. 2020HYGG04).

REFERENCES

Cao, W., Lin, L., Qi, H., He, Q., Wu, Z., Wang, A., et al. (2019). *In-situ* Synthesis of Single-Atom Ir by Utilizing Metal-Organic Frameworks: An Acid-Resistant Catalyst for Hydrogenation of Levulinic Acid to γ-valerolactone. *J. Catal.* 373, 161–172. doi:10.1016/j.jcat.2019.03.035

Chen, D., Liu, Z., Guo, Z., Ruan, M., and Yan, W. (2019). 3D Branched Ca-Fe 2 O 3/Fe 2 O 3 Decorated with Pt and Co-Pi: Improved Charge-Separation Dynamics and Photoelectrochemical Performance. *ChemSusChem* 12 (14), 3286–3295. doi:10.1002/cssc.201901331

Chen, P., Liu, F., Ding, H., Chen, S., Chen, L., Li, Y.-J., et al. (2019). Porous Double-Shell CdS@C3N4 Octahedron Derived by *In Situ* Supramolecular Self-Assembly for Enhanced Photocatalytic Activity. *Appl. Catal. B Environ.* 252, 33–40. doi:10.1016/j.apcatb.2019.04.006

Cheng, T., Gao, W., Gao, H., Wang, S., Yi, Z., Wang, X., et al. (2021). Piezocatalytic Degradation of Methylene Blue, Tetrabromobisphenol A and Tetracycline Hydrochloride Using Bi4Ti3O12 with Different Morphologies. *Mater. Res. Bull.* 141, 111350. doi:10.1016/j.materresbull.2021.111350

Cheng, T., Ma, Q., Gao, H., Meng, S., Lu, Z., Wang, S., et al. (2022). Enhanced Photocatalytic Activity, Mechanism and Potential Application of Idoped-Bi4Ti3O12 Photocatalysts. *Mater. Today Chem.* 23, 100750. doi:10.1016/j.mtchem.2021.100750

Chong, R., Wang, Z., Lv, J., Rong, J., Zhang, L., Jia, Y., et al. (2021). A Hybrid CoOOH-rGO/Fe2O3 Photoanode with Spatial Charge Separation and Charge Transfer for Efficient Photoelectrochemical Water Oxidation. *J. Catal.* 399, 170–181. doi:10.1016/j.jcat.2021.05.006

Dadashzadeh, A., Moghassemi, S., and Amorim, C. A. (2021). Evaluation of PEGylated Fibrin as a Three-Dimensional Biodegradable Scaffold for Ovarian Tissue Engineering. *Mater. Today Chem.* 22, 100626. doi:10.1016/j.mtchem.2021.100626

Dat, N. M., Thinh, D. B., Huong, L. M., Tinh, N. T., Linh, N. T. T., Hai, N. D., et al. (2022). Facile Synthesis and Antibacterial Activity of Silver Nanoparticles-Modified Graphene Oxide Hybrid Material: the Assessment, Utilization, and Anti-virus Potentiality. *Mater. Today Chem.* 23, 100738. doi:10.1016/j.mtchem.2021.100738

El-Hnayn, R., Canabady-Rochelle, L., Desmarets, C., Balan, L., Rinnert, H., Joubert, O., et al. (2020). One-step Synthesis of Diamine-Functionalized Graphene Quantum Dots from Graphene Oxide and Their Chelating and Antioxidant Activities. *Nanomaterials* 10 (1), 104. doi:10.3390/nano10010104

Fu, L., Yu, H., Lin, Y., and Fang, W. (2021). Nanowheat-Like α-Fe2O3@Co-Based/Ti Foil Photoanode with Surface Defects for Enhanced Charge Carrier Separation and Photoelectrochemical Water Splitting. *Energy fuels.* 35 (21), 17956–17963. doi:10.1021/acs.energyfuels.1c02763

Gao, H. J., Wang, S. F., Fang, L. M., Sun, G. A., Chen, X. P., Tang, S. N., et al. (2021). Nanostructured Spinel-type M(M = Mg, Co, Zn)Cr2O4 Oxides: Novel Adsorbents for Aqueous Congo Red Removal. *Mater. Today Chem.* 22, 100593. doi:10.1016/j.mtchem.2021.100593

Gao, H., Wang, F., Wang, S., Wang, X., Yi, Z., and Yang, H. (2019). Photocatalytic Activity Tuning in a Novel Ag2S/CQDs/CuBi2O4 Composite: Synthesis and Photocatalytic Mechanism. *Mater. Res. Bull.* 115, 140–149. doi:10.1016/j.materresbull.2019.03.021

Gao, H., Wang, S., Wang, Y., Yang, H., Wang, F., Tang, S., et al. (2022). CaMoO4/CaWO4 Heterojunction Micro/nanocomposites with Interface Defects for Enhanced Photocatalytic Activity. *Colloids Surfaces A Physicochem. Eng. Aspects* 642, 128642. doi:10.1016/j.colsurfa.2022.128642

Gao, H., Wang, Y., Wang, S., Yang, H., and Yi, Z. (2022). A Simple Fabrication, Microstructure, Optical, Photoluminescence and Supercapacitive Performances of MgMoO4/MgWO4 Heterojunction Micro/nanocomposites. *Solid State Sci.* 129, 106909. doi:10.1016/j.solidstatesciences.2022.106909

Gao, H., Yu, C., Wang, Y., Wang, S., Yang, H., Wang, F., et al. (2022). A Novel Photoluminescence Phenomenon in a SrMoO4/SrWO4 Micro/nano Heterojunction Phosphors Obtained by the Polyacrylamide Gel Method Combined with Low Temperature Calcination Technology. *J. Luminescence* 243, 118660. doi:10.1016/j.jlumin.2021.118660

Guskos, N., Zolnierkiewicz, G., Typek, J., Sibera, D., and Narkiewicz, U. (2010). Magnetic Resonance Study of ZnO-Fe2O3-ZnFe2O4 System. *Rev. Adv. Mater. Sci.* 23, 224–228. AvaliableAt: https://www.ipme.ru/e-journals/RAMS/no_22310/guskos8.pdf.

He, Z., Siddique, M. S., Yang, H., Xia, Y., Su, J., Tang, B., et al. (2022). Novel Z-Scheme In2S3/Bi2WO6 Core-Shell Heterojunctions with Synergistic Enhanced Photocatalytic Degradation of Tetracycline Hydrochloride. *J. Clean. Prod.* 339, 130634. doi:10.1016/j.jclepro.2022.130634

He, Z., Su, J., Chen, R., and Tang, B. (2019). Fabrication of Novel P-Ag2O/n-PbBiO2Br Heterojunction Photocatalysts with Enhanced Photocatalytic

Performance under Visible-Light Irradiation. *J. Mater Sci. Mater Electron* 30 (23), 20870–20880. doi:10.1007/s10854-019-02454-y

He, Z., Su, J., Xia, Y., and Tang, B. (2020). Fabrication and Photocatalytic Performance of Bi 24 O 31 Br 10 Nanosphere by a Polyacrylamide Gel Method. *Micro & Nano Lett.* 15 (8), 499–502. doi:10.1049/mnl.2020.0016

He, Z., Xia, Y., Su, J., and Tang, B. (2019). Fabrication of Magnetically Separable NiFe2O4/Bi24O31Br10 Nanocomposites and Excellent Photocatalytic Performance under Visible Light Irradiation. *Opt. Mater.* 88, 195–203. doi:10.1016/j.optmat.2018.11.025

He, Z., Yang, H., Su, J., Xia, Y., Fu, X., Kang, L., et al. (2021). Polyacrylamide Gel Synthesis and Photocatalytic Performance of CuCo2O4 Nanoparticles. *Mater. Lett.* 288, 129375. doi:10.1016/j.matlet.2021.129375

He, Z., Yang, H., Su, J., Xia, Y., Fu, X., Wang, L., et al. (2021). Construction of Multifunctional Dual Z-Scheme Composites with Enhanced Photocatalytic Activities for Degradation of Ciprofloxacin. *Fuel* 294, 120399. doi:10.1016/j.fuel.2021.120399

Hosseini, S. A., Abbasian, A. R., Gholipoor, O., Ranjan, S., and Dasgupta, N. (2019). Adsorptive Removal of Arsenic from Real Sample of Polluted Water Using Magnetic GO/ZnFe2O4 Nanocomposite and ZnFe2O4 Nanospinel. *Int. J. Environ. Sci. Technol.* 16 (11), 7455–7466. doi:10.1007/s13762-018-2140-x

Hwa, K. Y., Santhan, A., and Sharma, T. S. K. (2022). One-dimensional Self-Assembled Co2SnO4 Nanosphere to Nanocubes Intertwined in Two-Dimensional Reduced Graphene Oxide: an Intriguing Electrocatalytic Sensor toward Mesalamine Detection. *Mater. Today Chem.* 23, 100739. doi:10.1016/j.mtchem.2021.100739

Iliut, M., Gabudean, A.-M., Leordean, C., Simon, T., Teodorescu, C.-M., and Astilean, S. (2013). Riboflavin Enhanced Fluorescence of Highly Reduced Graphene Oxide. *Chem. Phys. Lett.* 586, 127–131. doi:10.1016/j.cplett.2013.09.032

Karpova, S. S., Moshnikov, V. A., Maksimov, A. I., Mjakin, S. V., and Kazantseva, N. E. (2013). Study of the Effect of the Acid-Base Surface Properties of ZnO, Fe2O3 and ZnFe2O4 Oxides on Their Gas Sensitivity to Ethanol Vapor. *Semiconductors* 47 (8), 1026–1030. doi:10.1134/S1063782613080095

Karpova, S. S., Moshnikov, V. A., Mjakin, S. V., and Kolovangina, E. S. (2013). Surface Functional Composition and Sensor Properties of ZnO, Fe2O3, and ZnFe2O4. *Semiconductors* 47 (3), 392–395. doi:10.1134/S1063782613030123

Kelaidis, N., Bousiadi, S., Zervos, M., Chroneos, A., and Lathiotakis, N. N. (2020). Electronic Properties of the Sn1-xPbxO Alloy and Band Alignment of the SnO/PbO System: a DFT Study. *Sci. Rep.* 10 (1), 16828–8. doi:10.1038/s41598-020-73703-y

Kormányos, A., Kecsenovity, E., Honarfar, A., Pullerits, T., and Janáky, C. (2020). Hybrid FeNiOOH/α-Fe 2 O 3/Graphene Photoelectrodes with Advanced Water Oxidation Performance. *Adv. Funct. Mat.* 30 (31), 2002124. doi:10.1002/adfm.202002124

Kuang, P., Zhang, L., Cheng, B., and Yu, J. (2017). Enhanced Charge Transfer Kinetics of Fe2O3/CdS Composite Nanorod Arrays Using Cobalt-Phosphate as Cocatalyst. *Appl. Catal. B Environ.* 218, 570–580. doi:10.1016/j.apcatb.2017.07.002

Li, J., Wang, S., Sun, G., Gao, H., Yu, X., Tang, S., et al. (2021). Facile Preparation of MgAl2O4/CeO2/Mn3O4 Heterojunction Photocatalyst and Enhanced Photocatalytic Activity. *Mater. Today Chem.* 19, 100390. doi:10.1016/j.mtchem.2020.100390

Li, L., Sun, X., Xian, T., Gao, H., Wang, S., Yi, Z., et al. (2022). Template-free Synthesis of Bi2O2CO3 Hierarchical Nanotubes Self-Assembled from Ordered Nanoplates for Promising Photocatalytic Applications. *Phys. Chem. Chem. Phys.* 24 (14), 8279–8295. doi:10.1039/D1CP05952A

Lin, X., Du, S., Li, C., Li, G., Li, Y., Chen, F., et al. (2020). Consciously Constructing the Robust NiS/g-C3n4 Hybrids for Enhanced Photocatalytic Hydrogen Evolution. *Catal. Lett.* 150 (7), 1898–1908. doi:10.1007/s10562-020-03118-x

Liu, H., Wang, S., Gao, H., Yang, H., Wang, F., Chen, X., et al. (2022). A Simple Polyacrylamide Gel Route for the Synthesis of MgAl2O4 Nanoparticles with Different Metal Sources as an Efficient Adsorbent: Neural Network Algorithm Simulation, Equilibrium, Kinetics and Thermodynamic Studies. *Sep. Purif. Technol.* 281, 119855. doi:10.1016/j.seppur.2021.119855

Luo, W., Cao, W., Bruijnincx, P. C. A., Lin, L., Wang, A., and Zhang, T. (2019). Zeolite-supported Metal Catalysts for Selective Hydrodeoxygenation of Biomass-Derived Platform Molecules. *Green Chem.* 21 (14), 3744–3768. doi:10.1039/C9GC01216H

Lv, A., Hu, C., Nie, Y., and Qu, J. (2010). Catalytic Ozonation of Toxic Pollutants over Magnetic Cobalt and Manganese Co-doped γ-Fe2O3. *Appl. Catal. B Environ.* 100 (1-2), 62–67. doi:10.1016/j.apcatb.2010.07.011

Nadeem, M. S., Munawar, T., Mukhtar, F., Naveed ur Rahman, M., Riaz, M., Hussain, A., et al. (2021). Hydrothermally Derived Co, Ni Co-doped ZnO Nanorods; Structural, Optical, and Morphological Study. *Opt. Mater.* 111, 110606. doi:10.1016/j.optmat.2020.110606

Pei, J., Zhao, H., Yang, F., and Yan, D. (2021). Graphene Oxide/Fe2O3 Nanocomposite as an Efficient Catalyst for Thermal Decomposition of Ammonium Perchlorate *via* the Vacuum-Freeze-Drying Method. *Langmuir* 37 (20), 6132–6138. doi:10.1021/acs.langmuir.1c00108

Prabhu, S., Pudukudy, M., Sohila, S., Harish, S., Navaneethan, M., Navaneethan, D., et al. (2018). Synthesis, Structural and Optical Properties of ZnO Spindle/reduced Graphene Oxide Composites with Enhanced Photocatalytic Activity under Visible Light Irradiation. *Opt. Mater.* 79, 186–195. doi:10.1016/j.optmat.2018.02.061

Rahmani, S., Seyed Dorraji, M. S., Rahmani, S., Hajimiri, I., and Amani-Ghadim, A. R. (2020). Loading GO/ZnFe2O4/NiO Nanocomposite as a Hybrid Dielectric/magnetic Material into Polyurethane Foam for Induction of Radar Absorbing Properties. *J. Mater Sci. Mater Electron* 31 (7), 5107–5116. doi:10.1007/s10854-020-03071-w

Rammah, Y. S., El-Agawany, F. I., Mahmoud, K. A., El-Mallawany, R., Ilik, E., and Kilic, G. (2020). FTIR, UV-Vis-NIR Spectroscopy, and Gamma Rays Shielding Competence of Novel ZnO-Doped Vanadium Borophosphate Glasses. *J. Mater Sci. Mater Electron* 31 (12), 9099–9113. doi:10.1007/s10854-020-03440-5

Rasheed, T. (2022). MXenes as Emerging Two-Dimensional Analytical Modalities for Potential Recognition of Hazardous Environmental Contaminants. *Mater. Today Chem.* 24, 100859. doi:10.1016/j.mtchem.2022.100859

Ratep, A., and Kashif, I. (2021). X-ray Photoelectron, FTIR, and Mössbauer Spectroscopy Studied the Effect of Fe2O3/CuO Substitution on Structural and Electrical Properties of Lithium Borosilicate Glasses. *J. Mater Sci. Mater Electron* 32 (9), 12340–12347. doi:10.1007/s10854-021-05865-y

Ren, L., Li, Y., Hou, J., Bai, J., Mao, M., Zeng, M., et al. (2016). The Pivotal Effect of the Interaction between Reactant and Anatase TiO2 Nanosheets with Exposed {0 0 1} Facets on Photocatalysis for the Photocatalytic Purification of VOCs. *Appl. Catal. B Environ.* 181, 625–634. doi:10.1016/j.apcatb.2015.08.034

Sadrameli, S. M. (2016). Thermal/catalytic Cracking of Liquid Hydrocarbons for the Production of Olefins: A State-Of-The-Art Review II: Catalytic Cracking Review. *Fuel* 173, 285–297. doi:10.1016/j.fuel.2016.01.047

Selli, E., Bianchi, C., Pirola, C., Cappelletti, G., and Ragaini, V. (2008). Efficiency of 1,4-dichlorobenzene Degradation in Water under Photolysis, Photocatalysis on TiO2 and Sonolysis. *J. Hazard. Mater.* 153 (3), 1136–1141. doi:10.1016/j.jhazmat.2007.09.071

Shanavas, S., Mohana Roopan, S., Priyadharsan, A., Devipriya, D., Jayapandi, S., Acevedo, R., et al. (2019). Computationally Guided Synthesis of (2D/3D/2D) rGO/Fe2O3/g-C3n4 Nanostructure with Improved Charge Separation and Transportation Efficiency for Degradation of Pharmaceutical Molecules. *Appl. Catal. B Environ.* 255, 117758. doi:10.1016/j.apcatb.2019.117758

Tang, N., Li, Y., Chen, F., and Han, Z. (2018). *In Situ* fabrication of a Direct Z-Scheme Photocatalyst by Immobilizing CdS Quantum Dots in the Channels of Graphene-Hybridized and Supported Mesoporous Titanium Nanocrystals for High Photocatalytic Performance under Visible Light. *RSC Adv.* 8 (73), 42233–42245. doi:10.1039/C8RA08008A

Tang, S., Fu, Z., Li, Y., and Li, Y. (2020). Study on Boron and Fluorine-Doped C3N4 as a Solid Activator for Cyclohexane Oxidation with H2O2 Catalyzed by 8-quinolinolato ironIII Complexes under Visible Light Irradiation. *Appl. Catal. A General* 590, 117342. doi:10.1016/j.apcata.2019.117342

Tang, S., Gao, H., Wang, S., Fang, L., Chen, X., Yang, H., et al. (2022). Piezoelectric Catalytic, Photocatalytic and Adsorption Capability and Selectivity Removal of Various Dyes and Mixed Dye Wastewater by ZnO Nanoparticles. *Mgc* (Preprint), 1–19. doi:10.3233/MGC-210150

Valenzuela, M. A., Bosch, P., Jiménez-Becerrill, J., Quiroz, O., and Páez, A. I. (2002). Preparation, Characterization and Photocatalytic Activity of ZnO, Fe_2O_3 and $ZnFe_2O_4$. *J. Photochem. Photobiol. A Chem.* 148 (1-3), 177–182. doi:10.1016/S1010-6030(02)00040-0

Wang, S., Gao, H., Jin, Y., Chen, X., Wang, F., Yang, H., et al. (2022). Defect Engineering in Novel Broad-Band Gap Hexaaluminate MAl12O19 (M=Ca, Sr, Ba)-Based Photocatalysts Boosts Near Ultraviolet and Visible Light-Driven

Photocatalytic Performance. *Mater. Today Chem.* 24, 100942. doi:10.1016/j.mtchem.2022.100942

Wang, S., Tang, S., Gao, H., Chen, X., Liu, H., Yu, C., et al. (2021). Microstructure, Optical, Photoluminescence Properties and the Intrinsic Mechanism of Photoluminescence and Photocatalysis for the BaTiO3, BaTiO3/TiO2 and BaTiO3/TiO2/CeO2 Smart Composites. *Opt. Mater.* 118, 111273. doi:10.1016/j.optmat.2021.111273

Wang, S., Tang, S., Yang, H., Wang, F., Yu, C., Gao, H., et al. (2022). A Novel Heterojunction ZnO/CuO Piezoelectric Catalysts: Fabrication, Optical Properties and Piezoelectric Catalytic Activity for Efficient Degradation of Methylene Blue. *J. Mater Sci. Mater Electron* 33 (9), 7172–7190. doi:10.1007/s10854-022-07899-2

Wang, X., Li, S., Chen, P., Li, F., Hu, X., and Hua, T. (2022). Photocatalytic and Antifouling Properties of TiO2-Based Photocatalytic Membranes. *Mater. Today Chem.* 23, 100650. doi:10.1016/j.mtchem.2021.100650

Wang, Y., Gao, H., Wang, S., Fang, L., Chen, X., Yu, C., et al. (2021). Facile Synthesis of BaMoO4 and BaMoO4/BaWO4 Heterostructures with Type -I Band Arrangement and Enhanced Photoluminescence Properties. *Adv. Powder Technol.* 32 (11), 4186–4197. doi:10.1016/j.apt.2021.09.028

Wang, Y., Gao, J., Liu, Y., Li, M., Zhang, M., He, G., et al. (2021). Facile Fabrication of ZnO Nanorods Modified Fe3O4 Nanoparticles with Enhanced Magnetic, Photoelectrochemical and Photocatalytic Properties. *Opt. Mater.* 111, 110608. doi:10.1016/j.optmat.2020.110608

Wang, Y., Yang, L., Zhang, Y., Zhang, H., and Wei, J. (2019). Magnetic Optical Properties, and Photocatalytic Activity of the ZnFe2O4 Nanoparticles for the Degradation of the RhB Dye in Wastewater: Effects of Metal Salt and Surface Morphology. *Russ. J. Phys. Chem.* 93 (13), 2771–2781. doi:10.1134/S0036024419130314

Xiao, L., Zhang, Q., Chen, P., Chen, L., Ding, F., Tang, J., et al. (2019). Copper-mediated Metal-Organic Framework as Efficient Photocatalyst for the Partial Oxidation of Aromatic Alcohols under Visible-Light Irradiation: Synergism of Plasmonic Effect and Schottky Junction. *Appl. Catal. B Environ.* 248, 380–387. doi:10.1016/j.apcatb.2019.02.012

Xiong, X., Wang, B., Zhu, W., Tian, K., and Zhang, H. (2018). A Review on Ultrasonic Catalytic Microbubbles Ozonation Processes: Properties, Hydroxyl Radicals Generation Pathway and Potential in Application. *Catalysts* 9 (1), 10. doi:10.3390/catal9010010

Xue, J., Fujitsuka, M., and Majima, T. (2019). Shallow Trap State-Induced Efficient Electron Transfer at the Interface of Heterojunction Photocatalysts: the Crucial Role of Vacancy Defects. *ACS Appl. Mat. Interfaces* 11 (43), 40860–40867. doi:10.1021/acsami.9b14128

Zhao, W., Xie, F., Gan, M., Ma, L., Zhang, Y., Li, X., et al. (2022). Highly Graphitized Carbon-Wrapped PtFeCo Alloy with Enhanced Durability and Activity toward Methanol Electro-Oxidation. *Mater. Today Chem.* 24, 100788. doi:10.1016/j.mtchem.2022.100788

Conflict of Interest: The authors declare that the research was conducted in the absence of any commercial or financial relationships that could be construed as a potential conflict of interest.

Publisher's Note: All claims expressed in this article are solely those of the authors and do not necessarily represent those of their affiliated organizations, or those of the publisher, the editors, and the reviewers. Any product that may be evaluated in this article, or claim that may be made by its manufacturer, is not guaranteed or endorsed by the publisher.